nature neuroscience

The exon junction complex component *Magoh* controls brain size by regulating neural stem cell division

Debra L Silver[1], Dawn E Watkins-Chow[1], Karisa C Schreck[2], Tarran J Pierfelice[2], Denise M Larson[1], Anthony J Burnetti[1], Hung-Jiun Liaw[3], Kyungjae Myung[3], Christopher A Walsh[4], Nicholas Gaiano[2] & William J Pavan[1]

Brain structure and size require precise division of neural stem cells (NSCs), which self-renew and generate intermediate neural progenitors (INPs) and neurons. The factors that regulate NSCs remain poorly understood, and mechanistic explanations of how aberrant NSC division causes the reduced brain size seen in microcephaly are lacking. Here we show that *Magoh*, a component of the exon junction complex (EJC) that binds RNA, controls mouse cerebral cortical size by regulating NSC division. *Magoh* haploinsufficiency causes microcephaly because of INP depletion and neuronal apoptosis. Defective mitosis underlies these phenotypes, as depletion of EJC components disrupts mitotic spindle orientation and integrity, chromosome number and genomic stability. *In utero* rescue experiments showed that a key function of *Magoh* is to control levels of the microcephaly-associated protein Lis1 during neurogenesis. Our results uncover requirements for the EJC in brain development, NSC maintenance and mitosis, thereby implicating this complex in the pathogenesis of microcephaly.

In humans, mice and flies, the size and structure of the adult brain depend on precise control of NSC division during development. NSCs, composed initially of neuroepithelial cells and then radial glia, are located in the ventricular zone bordering the ventricle of the neocortex[1]. NSCs undergo proliferative symmetric and asymmetric divisions to replenish themselves and to produce INPs, respectively. INPs, which reside next to the ventricular zone in the subventricular zone (SVZ), are thought to produce a majority of cortical neurons[2,3]. Neurons are also produced by NSCs undergoing neurogenic asymmetric divisions. Thus, a balance of symmetric and asymmetric NSC divisions regulates the number of NSCs, INPs and neurons produced and is critical for defining the adult brain. This balance may be influenced by both alterations in the NSC mitotic division plane and asymmetric inheritance of proteins that regulate cell fate[4–6]. The exact mechanisms that define NSC divisions remain, however, poorly understood.

Defects in NSC division can cause microcephaly, a congenital neurodevelopmental disorder characterized by markedly smaller brain size and cognitive deficiency of varying severity[7]. Microcephaly and microcephaly syndromes are associated with genes that regulate aspects of NSCs, including cell division and genomic integrity[8–10]. *CENPJ*, *ASPM* and *CDK5RAP2*, three genes associated with autosomal recessive microcephaly, encode proteins that regulate centrosomes, the microtubule organizing centers that anchor the mitotic spindle[8,9,11]. Increased and decreased dosages of Lis1, a microtubule-associated protein essential for mitotic spindle integrity, is associated with human microcephaly syndromes[12–14]. In addition, microcephaly-associated syndromes, Seckel syndrome and microcephalic osteodysplastic primordial dwarfism type II are caused by mutations in genes encoding centrosome and DNA damage signaling proteins[15–17]. Although studies of these genes highlight the fundamental role of mitosis in the etiology of microcephaly, very few genes are known to regulate both NSC mitosis and microcephaly *in vivo*. Thus, the genetic mechanisms regulating these processes are poorly defined. Here we have used a mouse mutant to explore how NSC aberrations cause microcephaly and to identify an essential regulator of NSC mitosis and brain size.

RESULTS

Magoh haploinsufficiency causes microcephaly

From an *N*-ethyl-*N*-nitrosourea (ENU) mutagenesis screen, we identified *Mos2* (Modifier of *Sox10*; ref. 18), a hypopigmented mouse mutant that is homozygous lethal before embryonic day 9.5 (E9.5) and heterozygous lethal with incomplete penetrance (**Table 1**). $Mos2^{+/-}$ mice were 33% smaller than control littermates ($P < 0.05$) but showed no significant differences in hematology, serum chemistry or histology of most organs (**Fig. 1a**, **Supplementary Table 1** and **Supplementary Data**). By contrast, $Mos2^{+/-}$ brains weighed significantly less than those of control littermates (0.234 g versus 0.509 g; $P < 0.05$) and were 28% smaller when normalized for overall reduced body size ($0.9 \pm 0.1\%$ versus $1.3 \pm 0.06\%$; **Fig. 1a** and **Supplementary Table 1**). These analyses demonstrate that $Mos2^{+/-}$ mice show reduced body size and microcephaly, in addition to hypopigmentation and premature death.

Linkage analysis using 573 backcrossed mice segregating the *Mos2* phenotypes defined a critical region of 2.4 Mb containing 38 annotated

[1]Genetic Disease Research Branch, National Human Genome Research Institute (NHGRI), National Institutes of Health (NIH), Bethesda, Maryland, USA. [2]Institute for Cell Engineering, Johns Hopkins University School of Medicine, Baltimore, Maryland, USA. [3]Genetics and Molecular Biology Branch, NHGRI, NIH, Bethesda, Maryland, USA. [4]Division of Genetics, Children's Hospital Boston and Departments of Pediatrics and Neurology, Harvard Medical School, Boston, Massachusetts, USA. Correspondence should be addressed to W.J.P. (bpavan@mail.nih.gov).

Received 14 December 2009; accepted 3 March 2010; published online 4 April 2010; corrected online 19 April 2010; doi:10.1038/nn.2527

genes (**Fig. 1b**). Sequence analysis of 12 genes in this interval identified one mutation (198delG) in the *Magoh* gene (NM_010760) that was not present in parental strains (**Fig. 1c**). *Magoh* encodes a component of the core EJC, which also contains RBM8A, EIF4A3 and CASC3 and binds spliced mRNA upstream of exon-exon junctions[19–23]. *Magoh* is highly conserved, showing 100% amino acid identity between mouse and human.

The $Magoh^{Mos2}$ allele is predicted to cause a frameshift resulting in a truncated protein. Immunoblot analyses of $Magoh^{Mos2/+}$ cortical lysates showed, however, smaller amounts of Magoh, but normal protein size (**Supplementary Fig. 1a**). Expression profile analysis of E10.5 cortices showed a 50% reduction in *Magoh* mRNA levels in $Magoh^{Mos2}$ as compared with control cortices ($P < 0.005$; **Supplementary Table 2**). This result was confirmed by quantitative gene expression analysis of control and $Magoh^{Mos2}$ cortices at E10.5 (normalized values: 0.91 ± 0.14 versus 0.45 ± 0.14) and E12.5 (0.81 ± 0.03 versus 0.52 ± 0.15; both $P < 0.0005$). Expression of the $Magoh^{Mos2}$ mutant allele was not detectable by restriction digestion or sequence analysis of real-time (RT)-PCR products (**Supplementary Fig. 1b**,**c**). Aberrantly sized RT-PCR products were also not observed, suggesting that abnormal splicing of the $Magoh^{Mos2}$ mutant transcript does not occur at high frequency in the neocortex (**Supplementary Fig. 1b**). Because the $Magoh^{Mos2}$ transcript contains a premature nonsense codon and was not detectable, we propose that the mutant allele undergoes nonsense mediated decay (NMD), a process dependent on EJC function. We cannot distinguish, however, whether NMD of *Magoh* occurs owing to degradation of a properly spliced mutant transcript or degradation of mis-spliced mRNA containing a premature termination codon.

Two approaches confirmed that mutation of *Magoh* caused the *Mos2* phenotypes. First, transgenic mice carrying either of two bacterial artificial chromosomes (BACs) expressing wild-type *Magoh* fully rescued the hypopigmentation, lethality, reduced body size and microcephaly phenotypes of $Magoh^{Mos2/+}$ mice (**Table 1** and **Supplementary Fig. 2**). Second, two independent *Magoh* mutant alleles, $Magoh^{GT0150/+}$ and $Magoh^{GT027/+}$, showed hypopigmentation, lethality, reduced body size and microcephaly, as seen in $Magoh^{Mos2/+}$ (**Fig. 1d**, **Table 1** and **Supplementary Fig. 2**). Taken together, the molecular and genetic evidence shows that $Magoh^{Mos2}$ is a null allele and that *Mos2*/+ phenotypes result from *Magoh* haploinsufficiency.

Table 1 Viability of *Magoh* mutants and BAC rescue

	Observed genotype[a]			
Genotype	Wild type	$Magoh^{Mos2/+}$	Tg-BAC; $Magoh^{+/+}$	Tg-BAC; $Magoh^{Mos2/+}$
$Magoh^{Mos2/+}$	90% (500)	10% (57)**	NA	NA
$Magoh^{Mos2/+}$ (E18.5)	50% (14)	50% (14)	NA	NA
$Magoh^{GT0150/+}$	89% (321)	11% (40)**	NA	NA
$Magoh^{GT027/+}$	93% (192)	7% (15)**	NA	NA
Tg-BAC1; $Magoh^{Mos2/+}$	37% (65)	0%	33% (58)	30% (51)**
Tg-BAC2; $Magoh^{Mos2/+}$	31% (84)	1% (3)	33% (88)	35% (96)**

[a]Percentage of viable offspring observed from mice of the indicated genotype crossed to wild type. Offspring were genotyped at weaning except where indicated (E18.5). The number of mice analyzed is given in parentheses.
NA, not applicable; $^{**}P < 0.001$.

Disorganized layers and fewer neurons in $Magoh^{Mos2/+}$ brains

Histological analysis of adult $Magoh^{Mos2/+}$ brains showed hypoplasia and global reduction of the cerebral cortex, corpus callosum and cerebellum (data not shown). The microcephaly was apparent prenatally, because the brains of E18.5 $Magoh^{Mos2/+}$ embryos were notably smaller and the cerebral cortex was disproportionately reduced in size (**Fig. 2a–f**). The cortical layers of E18.5 $Magoh^{Mos2/+}$ brains were thinner and somewhat disorganized (**Fig. 2c**,**f**). Cux1-positive neurons, produced late in neurogenesis and located in the outer layers of the cerebral cortex (layers II–IV), did not form a cohesive layer in $Magoh^{Mos2/+}$ brains (**Fig. 2g**,**h**,**k**,**l**). By contrast, older and deeper layers that are produced early in neurogenesis (layers V–VI), marked by Foxp1, Foxp2 and Tbr1, were present but markedly thinner in $Magoh^{Mos2/+}$ brains relative to controls (**Fig. 2i**,**j**,**m–v** and **Supplementary Fig. 3a**). $Magoh^{Mos2/+}$ E18.5 brains also contained 60% fewer Foxp1-, Foxp2- and Tbr1-positive neurons (**Supplementary Fig. 3b**). Overall, these analyses show that $Magoh^{Mos2/+}$ brains contain fewer neurons and that several neuronal layers are markedly affected.

Evaluation of younger $Magoh^{Mos2/+}$ embryos indicated that the onset of microcephaly occurs at approximately E12.5. E10.5 and E11.5 control and $Magoh^{Mos2/+}$ cortices showed a similar thickness and overall size, and were properly patterned, as assessed by *in situ* hybridization with *Wnt1*, *Gli3* and *Bmp4a*, early forebrain and midbrain markers (**Supplementary Fig. 3c** and data not shown). However, the cortical thickness of $Magoh^{Mos2/+}$ embryos was reduced by 10% at E12.5, 25% at E13.5, and 50% at E14.5 relative to controls. Consistent with a role in neurogenesis, Magoh protein expression was detected throughout the cortex from E11.5 to E16.5, a period that spans the onset and peak of neurogenesis (**Supplementary Fig. 1d**). At E14.5, *Magoh* mRNA expression was enriched in the ventricular zone and SVZ of the cortex, regions that are composed of NSCs and INPs (**Supplementary Fig. 1e**).

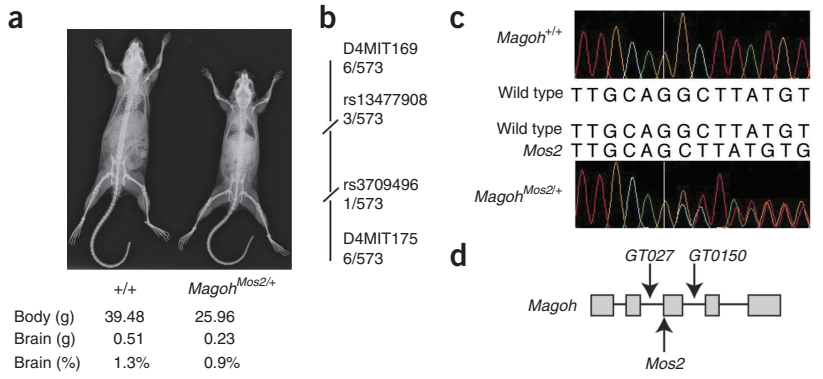

Figure 1 Mutation of *Magoh* causes microcephaly and reduced body size. (**a**) X-ray images of control and $Magoh^{Mos2/+}$ adult mice. Average body size, brain size and brain size as a percentage of total body weight are listed beneath each genotype. (**b**) Representation of linkage analysis on chromosome 4 with the indicated single-nucleotide polymorphisms and simple sequence length polymorphisms (bold) and the number of recombinants/meioses evaluated. For all markers shown, $P < 0.0005$. (**c**) Sequence chromatogram and corresponding sequences of control (top) and $Magoh^{Mos2/+}$ (bottom) genomic DNA. The $Magoh^{Mos2/+}$ DNA sequence contains a G deletion (right of the white line), and from this position onward, two peaks, representing the control and *Mos2* alleles, are apparent. (**d**) The *Magoh* gene, indicating exons (gray boxes), introns (lines, not drawn to scale) and the locations of three alleles.

Magoh is required for proper numbers of INPs

The *Magoh* expression pattern, combined with the neuronal depletion in *Magoh*$^{Mos2/+}$ embryos, suggested that the microcephaly reflects defects in NSCs and/or INPs (**Fig. 3**). At E13.5, E14.5 and E16.5, the density of Pax6-positive NSCs and thickness of the ventricular zone layer were similar in control and *Magoh*$^{Mos2/+}$ cortices (**Fig. 3a–f**,**o**,**p**). In contrast, the density of Tbr2-positive INPs of the SVZ and intermediate zone layers was markedly reduced in INPs in *Magoh*$^{Mos2/+}$ cortices at E13.5, E14.5 and E16.5 (**Fig. 3g–n**,**q**). Consistent with this, *Magoh*$^{Mos2/+}$ brains showed a 75% reduction in the total number of bromodeoxyuridine (BrdU)-positive cells in the SVZ and intermediate zone at E16.5 ($P < 0.005$; **Supplementary Fig. 4a**,**b**). The density of BrdU-positive cells remained the same, but the proportion of BrdU-positive cells expressing Tbr2 was significantly lower in *Magoh*$^{Mos2/+}$ cortices ($P < 0.05$; **Fig. 3i**,**j**,**m**,**n**,**r** and **Supplementary Fig. 4c**).

In support of these findings, both microarray and RT-PCR analyses showed that, in *Magoh*$^{Mos2/+}$ cortices, *Pax6* mRNA levels were normal, whereas mRNA levels for *Tbr2* (also known as *Eomes*) were reduced (**Supplementary Fig. 4d** and **Supplementary Table 2**). Together, these analyses indicate that *Magoh* is required for maintenance and/or generation of INPs. Because INPs produce a large fraction of neocortical neurons, this phenotype is consistent with the smaller number of neurons in E18.5 *Magoh*$^{Mos2/+}$ brains.

Ectopic neuron differentiation and apoptosis in *Magoh*$^{Mos2/+}$

The INP depletion in the *Magoh*$^{Mos2/+}$ brain suggested that the balance of asymmetric divisions might be disrupted, resulting in an increase in neuron production. To test this hypothesis, we evaluated new neuron production by monitoring expression of the neuronal markers Tuj1 and DCX (**Fig. 4**). At E10.5 and E11.5, no neuronal defects were observed in *Magoh*$^{Mos2/+}$ brains (**Supplementary Fig. 5a**,**b** and data not shown). Beginning at E12.5 and continuing through E13.5, however, the number of Tuj1- and DCX-positive cells was higher in *Magoh*$^{Mos2/+}$ (**Fig. 4a–d**,**g–j** and **Supplementary Fig. 5c–h**). This finding was confirmed by quantifying dissociated TuJ1-positive neurons of control and *Magoh*$^{Mos2/+}$ cortices (17.5 ± 3.3% versus 25.8 ± 5.7; $P < 0.0005$; **Fig. 4m**). Calretinin-positive cells were also expanded in number at E13.5 and E14.5, indicating that Cajal Retzius cells are ectopically produced in *Magoh*$^{Mos2/+}$ embryos (**Fig. 4e**,**f**,**k**,**l**). Consistent with these findings, the intermediate zone and cortical plate layers were significantly thicker in E13.5 *Magoh*$^{Mos2/+}$ embryos than in control embryos ($P < 0.005$; **Fig. 4n**). Together, these results indicate that *Magoh* is required to prevent ectopic and precocious neurogenesis.

Although E12.5 and E13.5 *Magoh*$^{Mos2/+}$ embryos contained ectopic neurons, E18.5 *Magoh*$^{Mos2/+}$ embryos had fewer neurons relative to control littermates, suggesting that the ectopic neurons did not survive. In *Magoh*$^{Mos2/+}$ but not control brains, we observed higher numbers of apoptotic cells (cleaved-caspase3 (CC3)- and TUNEL-positive) between the SVZ and cortical plate in a pattern similar to migratory neurons (**Fig. 4o–z** and **Supplementary Fig. 5a–f**). Colocalization of CC3 with Tuj1 and DCX confirmed that most of the dying cells were new neurons (**Fig. 4v**,**w** and **Supplementary Fig. 5**). By contrast, Tbr2-positive cells were TUNEL-negative, indicating that INPs did not undergo cell death (**Fig. 4r–t**,**x–z**). These results show that in *Magoh*$^{Mos2/+}$ embryos most ectopically produced neurons undergo cell death. In summary, we conclude that the microcephaly in *Magoh*$^{Mos2/+}$ cortices is due to both an increase in neuronal apoptosis and depletion of the neuron-producing INP population.

Magoh and core EJC components regulate the mitotic spindle

In microcephaly mutants such as *Lis1*$^{hc/ko}$ (also known as *Pafah1b1*$^{hc/ko}$), NSC and INP depletion, ectopic neurogenesis and neuronal apoptosis are associated with abnormal orientation of the NSC mitotic division plane[24–26]. In E10.5 *Magoh*$^{Mos2/+}$ embryos, evaluation of dividing cells with phospho-histone H3 (PH3) showed no defects in division or PH3 number (**Supplementary Fig. 6a**,**b**). At E11.5 and E12.5, however, the number of intermediate and horizontal divisions was significantly higher in *Magoh*$^{Mos2/+}$ embryos ($P < 0.005$ and $P < 0.05$,

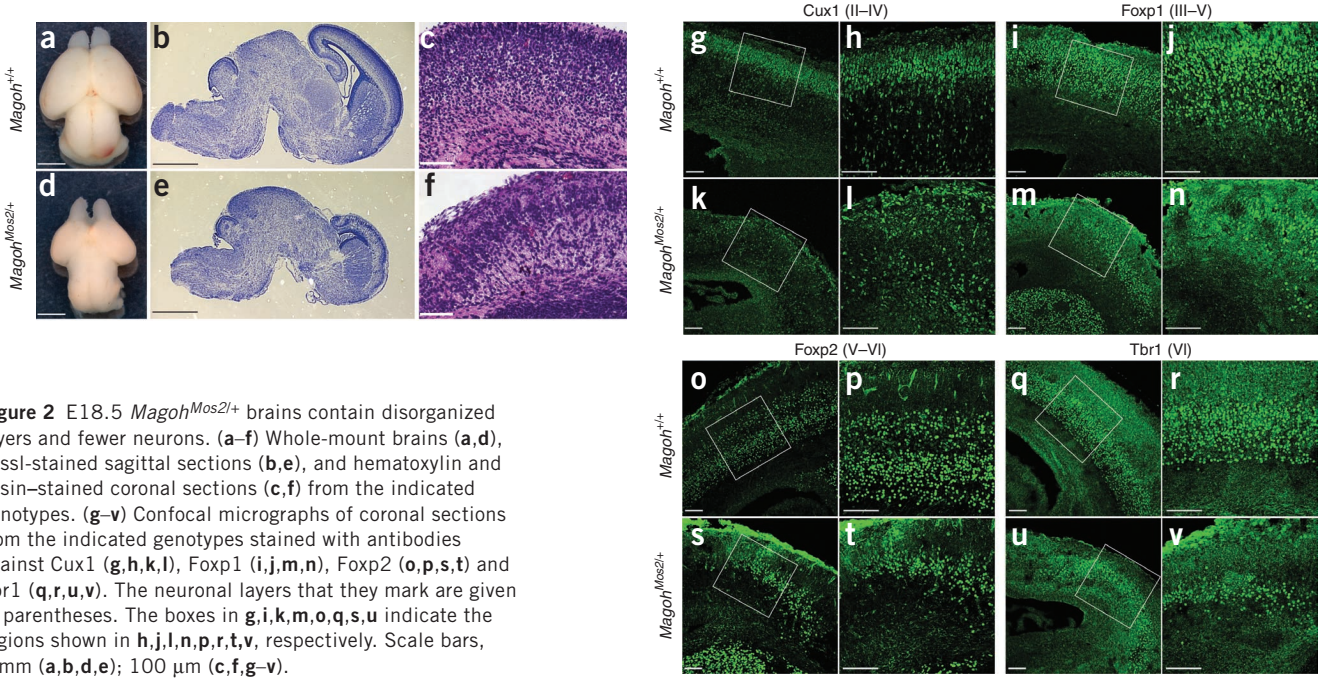

Figure 2 E18.5 *Magoh*$^{Mos2/+}$ brains contain disorganized layers and fewer neurons. (**a**–**f**) Whole-mount brains (**a**,**d**), Nissl-stained sagittal sections (**b**,**e**), and hematoxylin and eosin–stained coronal sections (**c**,**f**) from the indicated genotypes. (**g**–**v**) Confocal micrographs of coronal sections from the indicated genotypes stained with antibodies against Cux1 (**g**,**h**,**k**,**l**), Foxp1 (**i**,**j**,**m**,**n**), Foxp2 (**o**,**p**,**s**,**t**) and Tbr1 (**q**,**r**,**u**,**v**). The neuronal layers that they mark are given in parentheses. The boxes in **g**,**i**,**k**,**m**,**o**,**q**,**s**,**u** indicate the regions shown in **h**,**j**,**l**,**n**,**p**,**r**,**t**,**v**, respectively. Scale bars, 1 mm (**a**,**b**,**d**,**e**); 100 μm (**c**,**f**,**g**–**v**).

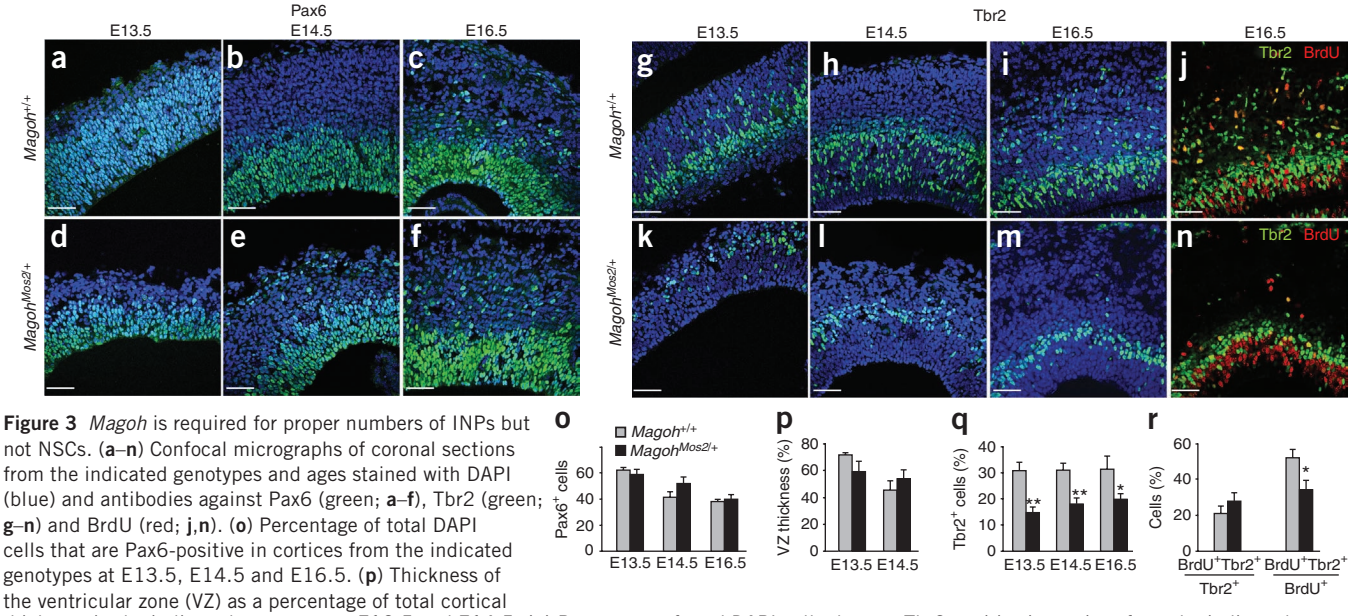

Figure 3 *Magoh* is required for proper numbers of INPs but not NSCs. (**a**–**n**) Confocal micrographs of coronal sections from the indicated genotypes and ages stained with DAPI (blue) and antibodies against Pax6 (green; **a**–**f**), Tbr2 (green; **g**–**n**) and BrdU (red; **j**,**n**). (**o**) Percentage of total DAPI cells that are Pax6-positive in cortices from the indicated genotypes at E13.5, E14.5 and E16.5. (**p**) Thickness of the ventricular zone (VZ) as a percentage of total cortical thickness in the indicated genotypes at E13.5 and E14.5. (**q**) Percentage of total DAPI cells that are Tbr2-positive in cortices from the indicated genotypes at E13.5, E14.5 and E16.5. (**r**) Percentage of Tbr2-positive cells that are BrdU-positive (left) and percentage of BrdU-positive cells that are Tbr2-positive (right). Pregnant females were dissected 1 h after BrdU injection. For **o**–**r**, the average values for all embryos ($n = 2$–4 per genotype, four to five sections per embryo) is shown, quantified within a 318-μm^2 field. $^*P < 0.05$, $^{**}P < 0.005$; no asterisk indicates no significant differences were observed. Error bars, s.d.; scale bars, 50 μm.

respectively; **Fig. 5a**,**b**). The onset of this spindle defect at E11.5, before massive apoptosis or premature differentiation, suggests that the spindle defect is not an artifact of general tissue disorganization (**Supplementary Fig. 5i–l**). Thus, we conclude that *Magoh* is required for proper orientation of the NSC mitotic division plane.

The apoptosis of *Magoh*$^{Mos2/+}$ neurons might result from aberrant chromosome numbers owing to defective NSC division. Consistent with this theory, metaphase analysis indicated that *Magoh*$^{Mos2/+}$ mouse embryonic fibroblasts (MEFs) had twice as many polyploid cells as did controls ($P < 0.0005$; **Fig. 5c**). Spectral karyotyping (SKY) analysis of metaphase spreads also showed more chromosomal aneuploidy in *Magoh*$^{Mos2/+}$ MEFs as compared with controls ($P < 0.0005$; **Fig. 5d**). Aneuploidy was random relative to the number and type of chromosomes affected. These results demonstrate that *Magoh* is required to maintain chromosome number during mitosis.

To evaluate further the requirement of *Magoh* for cell division, siRNA knockdown in HeLa cells was used to deplete Magoh protein

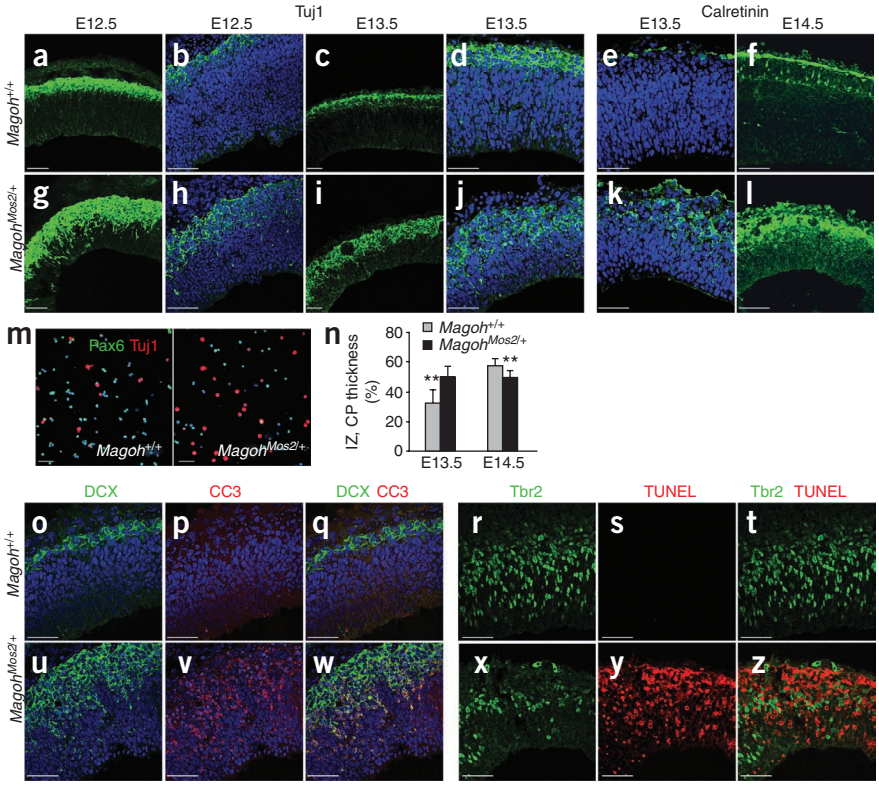

Figure 4 *Magoh* is required to prevent premature neuronal differentiation and apoptosis. (**a**–**l**) Low-magnification (**a**,**c**,**g**,**i**) and high-magnification (**b**,**d**,**e**,**f**,**h**,**j**–**l**) confocal micrographs of coronal sections from the indicated genotypes and ages, stained for Tuj1 (green) and DAPI (blue; **a**–**d**,**g**–**j**), or Calretinin (green) and DAPI (blue; **e**,**f**,**k**,**l**). (**m**) Confocal micrographs of dissociated E12.5 cortical cells from the indicated genotypes stained for Pax6 (green), Tuj1 (red) and DAPI (blue). (**n**) Thickness of the cortical plate and intermediate zone together as a percentage of total cortical thickness. The average value for all embryos ($n = 3$–4 per genotype, four to five sections per embryo) is shown, quantified within a 318-μm^2 field. (**o**–**z**) Confocal micrographs of E12.5 coronal sections (**o**–**q**,**u**–**w**) of the indicated genotypes stained for DCX (green; **o**,**u**), CC3 (red; **p**,**v**), or DCX (green) and CC3 (red; **q**,**w**), and E14.5 coronal sections (**r**–**t**,**x**–**z**) of the indicated genotypes stained for Tbr2 (green; **r**,**x**), TUNEL (red; **s**,**y**), or Tbr2 (green) and TUNEL (red; **t**,**z**). $^{**}P < 0.005$. Error bars, s.d.; scale bars, 50 μm.

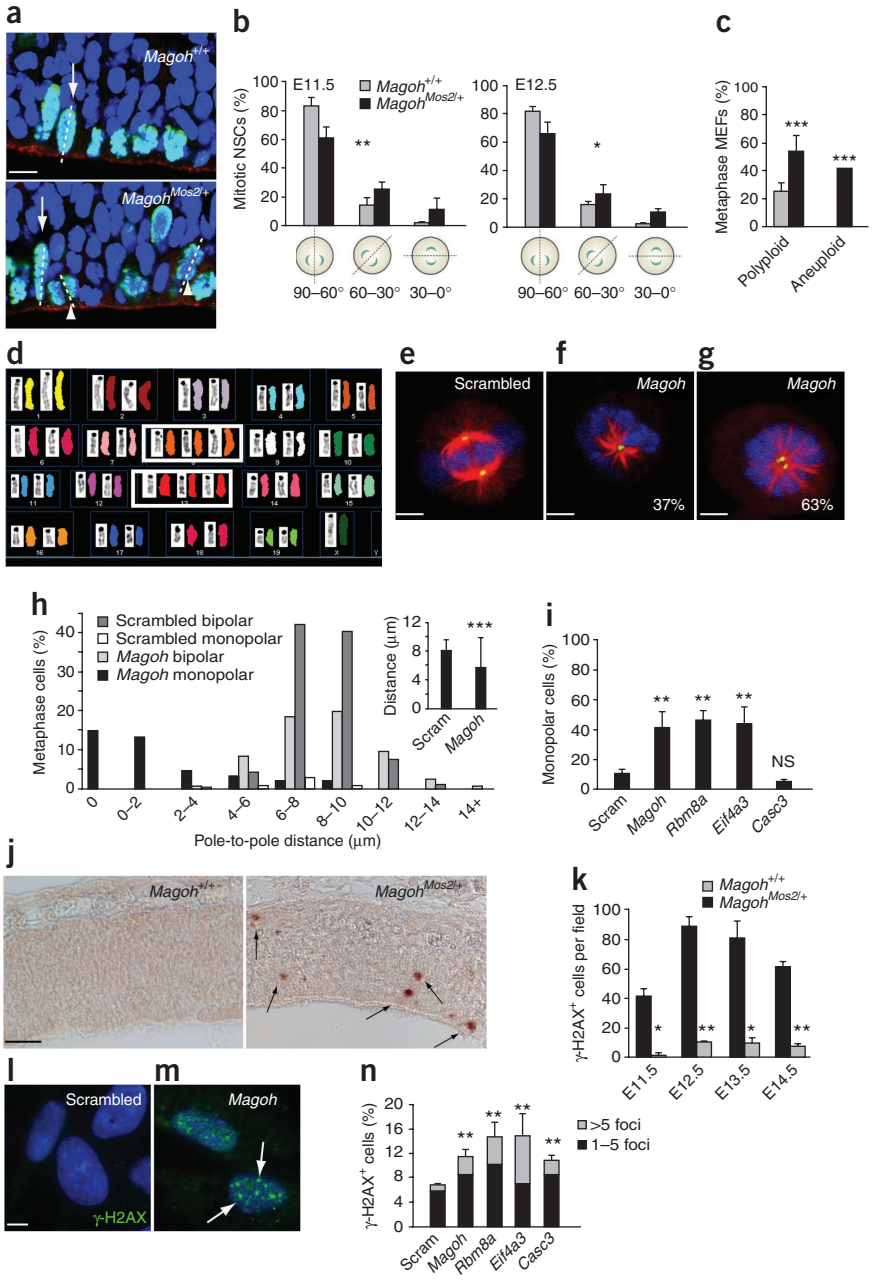

Figure 5 *Magoh* and core EJC components regulate the mitotic spindle, ploidy, mitosis and genomic stability. (**a**) Confocal micrographs of E11.5 coronal sections stained with DAPI (blue) and rhodamine phalloidin (red), and for PH3 (green). Metaphase cells dividing vertically (arrows) and those with intermediate orientation (arrowheads) are indicated. (**b**,**c**) Percentage of NSCs showing the indicated mitotic cleavage planes at E11.5 (left, **b**) and E12.5 (right, **b**), and MEFs showing polyploidy and aneuploidy (**c**). (**d**) Representative SKY image from a $Magoh^{Mos2/+}$ MEF showing aneuploidy (three copies of chromosomes 8 and 13). (**e**–**g**) Confocal micrographs of HeLa cells treated with scrambled (**e**) and *Magoh* (**f**,**g**) siRNA, and stained with DAPI (blue) for α-tubulin (red) and γ-tubulin (green). Percentages indicate *Magoh* siRNA-treated monopolar cells containing one (**f**) or two (**g**) centrosomes. (**h**) Percentages of siRNA-treated metaphase cells showing the indicated pole-to-pole distances. Bipolar and monopolar cells are shown independently (left) and together (inset). (**i**) Percentages of siRNA-treated cells that are monopolar. (**j**) Images of E11.5 coronal sections stained for γ-H2AX (brown, arrows). (**k**) Number of γ-H2AX–positive cells at the indicated ages. (**l**,**m**) Images of siRNA-treated RPE cells stained with DAPI (blue) and for γ-H2AX-positive foci (green, arrows). (**n**) Percentages of siRNA-treated RPE cells showing >5 γ-H2AX–positive and 1–5 γ-H2AX–positive foci. Graphs indicate average values for two to four embryos per genotype (**b**,**c**,**k**), for all siRNA-treated cells (**h**), and for three to six independent experiments (**i**,**n**). $*P < 0.05$, $**P < 0.005$, $***P < 0.0005$. Error bars, s.d. Scale bars, 5 μm (**e**–**g**), 10 μm (**a**,**m**), 50 μm (**l**).

(**Supplementary Fig. 6c**). Analysis of the mitotic spindle with α-tubulin revealed that 42% of dividing *Magoh* knockdown cells failed to form a bipolar spindle and instead showed an apparent monopolar spindle ($P < 0.005$; **Fig. 5e–i**). Because spindle defects are frequently caused by dysfunctional centrosomes, we assessed centrosome number and integrity using γ-tubulin, a pericentriolar marker of centrosomes. In *Magoh* knockdown cells, the average centrosome distance was smaller (5.78 μm versus 8.1 μm in controls, $P < 0.0005$; **Fig. 5h**). Of the cells showing monopolar spindles, 37% contained a single centrosome and spindle, indicating these were *bona fide* monopolar spindles (**Fig. 5f**,**h**). Of the cells with monopolar spindles, 63% contained two adjacently located centrosomes, most of which were less than 4 μm apart (**Fig. 5g**,**h** and **Supplementary Fig. 6d**). Knockdown of the other core EJC components *Rbm8a* and *Eif4a3*, but not *Casc3*, caused spindle defects similar to those observed for *Magoh* knockdown ($P < 0.005$, $P < 0.005$ and $P = 0.065$, respectively; **Fig. 5i**). Using fluorescence-activated cell sorting (FACS), we observed an average doubling in the proportion of cells in G2/M phases, confirming the disruption of mitosis (**Supplementary Fig. 7a**). Together, these data show that EJC components are required for cells to proceed from prophase into metaphase, for proper centrosome number and separation, and for integrity of the bipolar mitotic spindle.

Given the widespread apoptosis in $Magoh^{Mos2/+}$ embryos, and involvement of microcephaly-associated genes in DNA damage repair[10,15], we evaluated whether *Magoh* is required for genome stability by using the double-stranded break marker γ-H2AX. In contrast to control brains, in $Magoh^{Mos2/+}$ brains, the number of γ-H2AX-positive cells was significantly higher between E11.5 and E14.5 ($P < 0.05$ and $P < 0.005$; **Fig. 5j**,**k** and **Supplementary Fig. 7b**). We extended this analysis to assess the role of additional EJC components in genome stability using siRNA depletion in retinal pigment epithelial (RPE) cells. Reduced expression of *Magoh*, *Eif4a3*, *Rbm8a* and *Casc3* each resulted in a significant increase in DNA damage foci (**Fig. 5l**,**m**,**n** and **Supplementary Fig. 7c**). Taken together, these analyses show that components of the EJC are required for mitosis and DNA integrity, two processes that are disrupted in microcephaly.

Magoh acts upstream of Lis1 to regulate neurogenesis

Similar to $Magoh^{Mos2/+}$ mutants, $Lis1^{-/-}$ mutants show microcephaly, altered NSC mitotic cleavage planes, precocious neurogenesis, an

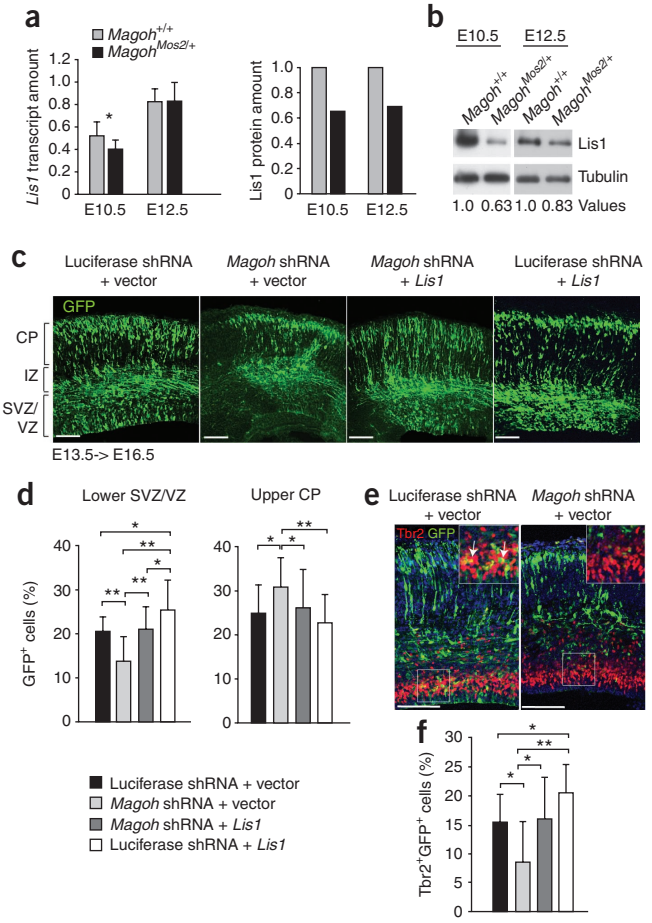

Figure 6 *Magoh* acts upstream of the microcephaly-associated protein Lis1 to regulate neurogenesis. (**a**) Graphs representing *Lis1* gene expression measured by quantitative PCR (left) and Lis1 protein expression measured from immunoblot analyses (right). (**b**) Representative cropped immunoblots of cortical lysates from the indicated ages and genotypes, probed with antibodies to Lis1 (46 kDa) and to α-tubulin (55 kDa) as a loading control. Below the lanes are the densitometry values normalized to a loading control set at 1.0 (see **Supplementary Fig. 8e** for the full-length blots). (**c**) Confocal micrographs of coronal sections from E16.5 brains *in utero* co-electroporated at E13.5 with pCAG-GFP (green) and the following: luciferase shRNA plus empty vector, *Magoh* shRNA plus empty vector, *Magoh* shRNA plus *Lis1*, and luciferase shRNA plus *Lis1*. In the *Magoh* shRNA plus empty vector brains, there are fewer GFP-positive cells in the SVZ/ventricular zone (VZ) layers. IZ, intermediate zone; CP, cortical plate. (**d**) Percentage of GFP-positive cells in lower SVZ/VZ and upper CP layers of the brain for the indicated *in utero* electroporations. (**e**) Confocal micrographs of brains from the indicated *in utero* electroporations showing GFP (green) and stained for Tbr2 (red) and DAPI (blue). Insets show a higher magnification view of the boxed region, highlighting colocalization (yellow) of Tbr2 (red) and GFP (green). (**f**) Percentage of GFP-positive cells expressing Tbr2 for the indicated *in utero* electroporations. Graphs in **d** and **f** show the average values of all sections. $*P < 0.05$, $**P < 0.005$. Error bars, s.d. Scale bars, 100 μm.

increase in apoptosis and a reduction in neural progenitors[24–26]. Given the role of the EJC in transcript regulation, and similarities between *Magoh* and *Lis1* mutant phenotypes, we hypothesized that *Magoh* might regulate brain size, in part, by controlling Lis1 expression. Inspection of *Lis1* mRNA levels in $Magoh^{Mos2/+}$ cortices showed minimal changes at E10.5 (22% reduced) and no changes at E12.5 (**Fig. 6a**). By contrast, immunoblot analyses showed that the amount of Lis1 protein was reduced in both $Magoh^{Mos2/+}$ E10.5 (34%) and E12.5 (30%) cortices (**Fig. 6b** and **Supplementary Fig. 8a**). A significant reduction in Lis1 protein was also independently detected by quantitative two-dimensional (2D) gel analysis of mutant E12.5 cortices (20% reduction; $P < 0.00005$) and by immunoblot analyses of *Magoh*-knockdown HeLa cells (50% reduction; **Supplementary Fig. 8b** and data not shown). These changes in Lis1 expression were not reflective of global alterations in steady-state mRNA and protein levels in E10.5 $Magoh^{Mos2/+}$ cortices, because expression profile analysis identified only 147 transcripts (0.8% of genes on the microarray) with altered levels ($P < 0.05$; **Supplementary Table 2**). Most of these changes were less than twofold higher or lower, indicating that the expression changes observed were not substantial. In addition, 2D gel analyses uncovered only eight significantly altered proteins (0.4%; $P < 0.05$). Consistent with our quantitative RT-PCR analyses, the mutant to wild-type ratio of *Lis1* mRNA detected by microarray was 0.85 ($P = 0.1166$). Thus, *Magoh* is required for proper expression of Lis1 protein, suggesting that altered amounts of Lis1 might account for some of the phenotypes resulting from *Magoh* haploinsufficiency.

We tested this hypothesis by determining whether *Lis1* expression is sufficient to rescue phenotypes associated with *Magoh* loss of function. We used *in utero* electroporation to introduce green fluorescent protein (GFP) along with either *Magoh* short hairpin RNA (shRNA) or luciferase shRNA (control) into E13.5 cortices, and then analyzed the distribution of GFP-positive cells at E16.5. GFP-positive cells in control electroporated brains showed a relatively even distribution throughout the cortical plate, intermediate zone and SVZ/ventricular zone layers (**Fig. 6c**,**d** and **Supplementary Fig. 8c**). In *Magoh* shRNA electroporated brains, however, there were significantly more GFP-positive cells in the upper cortical plate layer and significantly fewer in the lower SVZ/ventricular zone layer ($P < 0.05$ and $P < 0.005$, respectively; **Fig. 6c**,**d**), consistent with the neurogenesis defects observed in $Magoh^{Mos2/+}$ cortices. We observed similar distribution defects both on knockdown with two additional shRNA constructs against *Magoh* and on knockdown with different dosages of *Magoh* shRNA, further demonstrating the specificity of these phenotypes (data not shown and **Supplementary Fig. 8d**). The proportion of cells electroporated with *Magoh* shRNA that were Tbr2-positive was also significantly smaller than that in controls ($P < 0.05$; **Fig. 6e**,**f**). These results indicate that *in utero* knockdown of *Magoh* recapitulates the depletion of INPs in $Magoh^{Mos2/+}$ brains.

Next, we evaluated whether *Lis1* expression could rescue defects caused by *Magoh* knockdown. Brains co-electroporated with a *Lis1* expression vector and *Magoh* shRNA showed a even distribution of GFP-positive cells throughout the cortex, similar to control brains (**Fig. 6c**,**d** and **Supplementary Fig. 8c**). The distribution in the upper cortical plate and lower SVZ/ventricular zone layers was significantly different from that in brains electroporated with *Magoh* shRNA alone ($P < 0.05$ and $P < 0.005$, respectively), indicating that *Lis1* expression rescued the altered distribution caused by *Magoh* knockdown (**Fig. 6c**,**d**). Also consistent with a genetic relationship, an increase in GFP-positive cells in the SVZ/ventricular zone seen with *Lis1* expression alone[12] was abrogated in the co-electroporated brains (**Fig. 6c**,**d** and **Supplementary Fig. 8c**). *Lis1* and *Magoh* shRNA co-electroporation also rescued the loss of Tbr2-positive cells (**Fig. 6e**,**f**). Together, these results demonstrate that *Lis1* is sufficient to restore *Magoh*-depleted cells to their proper distribution and fate, *Magoh* is a critical regulator of Lis1 levels, and Lis1 is one of the key downstream targets of *Magoh* that regulates brain development.

DISCUSSION

Despite the fundamental importance of the core EJC in regulating RNA metabolism, the requirement of EJC components in vertebrate

development has not been evaluated. Here we used mouse genetics to uncover a cellular requirement for the EJC in mitosis and to show that mutation of *Magoh* disrupts brain size as a result of defective NSC division, INP depletion and neuronal apoptosis. Our study indicates that *Magoh* is an essential regulator of stem cell maintenance and division, and thus it has implications not only for microcephaly syndromes, but also for chromosome integrity and stem cell disorders such as cancer.

We have demonstrated that core EJC components regulate mitosis by modulating mitotic spindle integrity, in part by regulating centrosome separation and duplication. Components of the EJC, however, may also control mitotic spindle integrity by regulating microtubule organization, as in *Drosophila* oogenesis where the *Magoh* ortholog *mago* is required for microtubule polarization[27]. Together, these findings indicate that core EJC components have a fundamental and conserved, but largely unexplored, role in microtubule organization and cell division.

The requirement for the EJC in mitosis is manifested as altered chromosome number and loss of genome integrity. The observed polyploidy and aneuploidy are consistent with defects in centrosomes and mitotic progression. Delays in mitotic progression also probably explain the increased frequency of spontaneous DNA damage. Of note, depletion of the NMD component *UPF1* also increases DNA damage, but does so by disrupting DNA replication[28]. Although we cannot rule out a similar role for the EJC in replication, there is no evidence of an association of the core EJC with DNA and we found no evidence of an increase in S phase cells on loss of EJC components, as measured by FACS analysis or by BrdU incorporation in E16.5 brains. Thus, our working model is that defects in mitosis precede and result in an accumulation of DNA damage.

We propose that defective mitosis alters cell fates and causes microcephaly in $Magoh^{Mos2/+}$ mice. Either misoriented or dysfunctional mitotic spindles may interfere with production and/or maintenance of INPs and neurons by altering the distribution of fate determinants[4,6]. Hence, we predict that neuronal apoptosis is caused by inheritance of aberrant chromosome number and/or damaged DNA. The observed alterations in cell fate are also consistent with an overall shift in the balance of asymmetric, proliferative and neurogenic NSC divisions (**Supplementary Fig. 9**). Notably, this function is conserved across kingdoms, because knockdown of *mago* in spermatogenesis of the plant *Marsilea* skews the balance of symmetric and asymmetric cell divisions[29].

A key regulator of mitosis is Lis1, and our analyses indicate that an essential function of *Magoh* in brain development is to regulate amounts of Lis1 protein. The microarray, quantitative real-time PCR and immunoblot analyses together showed that, in *Magoh* mutants, Lis1 protein is reduced more significantly than is *Lis1* mRNA. This finding suggests that *Magoh* may regulate Lis1 protein expression, an observation consistent with the role established for Magoh and the EJC in regulating protein translation[19,22]. Hypomorphic or hypermorphic *Lis1* levels disrupt neurogenesis, leading to microcephaly[12,25,30]. We have shown that restoring normal Lis1 levels is sufficient to rescue the neurogenesis phenotypes affecting cellular distribution and progenitor number caused by *Magoh* knockdown. Consistent with a genetic relationship, $Magoh^{Mos2/+}$ and $Lis1^{-/-}$ mutants have similar phenotypes[24,25]. A few differences exist, such as the onset of spindle orientation defects, which is evident at E9.5 in $Lis1^{-/-}$ but is first evident at E11.5 in $Magoh^{Mos2/+}$ (ref. 26). However, the *Mos2* mutation is heterozygous and causes Lis1 reduction, but not loss; thus, the difference in mutant phenotypes may be due to Lis1 dosage.

It is important to note that *Magoh* mutants also show cellular phenotypes that have not previously been associated with *Lis1* function, including an increase in Cajal-Retzius cells, DNA damage and ploidy. These observations may indicate potentially new roles for Lis1, particularly in genomic stability. Alternatively, these *Magoh* mutant phenotypes may be due to the dysregulation of other critical targets of *Magoh*. Our electroporation experiment showed that Lis1 is a critical target of *Magoh* in generating progenitors between E13.5 and E16.5. It is unlikely, however, that Lis1 is the only critical target of *Magoh*, but rather that the complex process of neurogenesis that initiates before E13.5 is dependent on additional downstream genes. Future studies will reveal, for example, whether any of the genes altered in our microarray or proteomics experiments are also essential targets of *Magoh*.

Our findings implicate core EJC components in the pathogenesis of microcephaly syndromes. Of note, *MAGOH* is found within a 55-gene deletion on chromosome 1p32.3 that is associated with mental retardation and abnormalities in brain size[31]. In addition, *RBM8A* is one of 15 genes in a 0.4-Mb microdeletion on 1q21.1 that is associated with microcephaly[32,33]. Therefore, the core EJC functions that we have uncovered will open up a fruitful area of research into the role of this complex in brain development and disease, stem cell maintenance and chromosome anomaly disorders such as cancer.

METHODS

Methods and any associated references are available in the online version of the paper at http://www.nature.com/natureneuroscience/.

Accession codes. Microarray data have been deposited in the Gene Expression Omnibus under accession code GSE 19168.

Note: Supplementary information is available on the Nature Neuroscience website.

ACKNOWLEDGMENTS

For advice, we thank Pavan laboratory members, including L. Baxter for reading the manuscript. For technical assistance, we thank A. Incao (mouse husbandry); G. Elliot and A. Chen (mouse transgenics); A. Dutra, E. Pak and S. Witchovitch (metaphase, SKY, microscopy assistance); S. Anderson and M. Kirby (FACS analysis); B. Bhorate (microarray statistics); M. Bryant (pathology analysis); Harvard Partners Center for Genetics and Genomics (candidate gene sequencing); and J. Fekecs and D. Leja (assistance with figures). This research was funded in part by an National Institute of General Medical Sciences PRAT fellowship and K99/R00 Pathway to Independence Award (to D.L.S.), by the Intramural Research program of NIH/NHGRI (to W.J.P., K.M.) and by the NIH/NHGRI (to N.G.). C.A.W. is an Investigator of the Howard Hughes Medical Institute.

AUTHOR CONTRIBUTIONS

D.L.S. designed the study, performed all experiments except where noted otherwise and wrote the paper. D.E.W.-C. performed all mRNA analyses and assisted with quantitative analyses. K.C.S. and T.J.P. performed all *in utero* electroporations and dissections of electroporated brains. D.M.L. performed staining of E18.5 markers. A.J.B. assisted with HeLa cell analyses and quantification of NSCs and INPs. H.L. performed RPE cell analyses. D.L.S., W.J.P., C.A.W., N.G. and K.M. were involved in research design, and all authors were involved in data analysis. D.L.S. and W.J.P. prepared the manuscript. All authors have agreed to the content in the manuscript, including the data as presented.

COMPETING FINANCIAL INTERESTS

The authors declare no competing financial interests.

Published online at http://www.nature.com/natureneuroscience/.
Reprints and permissions information is available online at http://npg.nature.com/reprintsandpermissions/.

1. Molyneaux, B.J., Arlotta, P., Menezes, J.R. & Macklis, J.D. Neuronal subtype specification in the cerebral cortex. *Nat. Rev. Neurosci.* **8**, 427–437 (2007).
2. Haubensak, W., Attardo, A., Denk, W. & Huttner, W.B. Neurons arise in the basal neuroepithelium of the early mammalian telencephalon: a major site of neurogenesis. *Proc. Natl. Acad. Sci. USA* **101**, 3196–201 (2004).
3. Pontious, A., Kowalczyk, T., Englund, C. & Hevner, R.F. Role of intermediate progenitor cells in cerebral cortex development. *Dev Neurosci* **30**, 24–32 (2008).

4. Chenn, A. & McConnell, S.K. Cleavage orientation and the asymmetric inheritance of Notch1 immunoreactivity in mammalian neurogenesis. *Cell* **82**, 631–641 (1995).
5. Sanada, K. & Tsai, L.H. G protein βγ subunits and AGS3 control spindle orientation and asymmetric cell fate of cerebral cortical progenitors. *Cell* **122**, 119–131 (2005).
6. Zhong, W., Feder, J.N., Jiang, M.M., Jan, L.Y. & Jan, Y.N. Asymmetric localization of a mammalian numb homolog during mouse cortical neurogenesis. *Neuron* **17**, 43–53 (1996).
7. Bond, J. & Woods, C.G. Cytoskeletal genes regulating brain size. *Curr. Opin. Cell Biol.* **18**, 95–101 (2006).
8. Bond, J. *et al.* ASPM is a major determinant of cerebral cortical size. *Nat. Genet.* **32**, 316–320 (2002).
9. Bond, J. *et al.* A centrosomal mechanism involving CDK5RAP2 and CENPJ controls brain size. *Nat. Genet.* **37**, 353–355 (2005).
10. Jackson, A.P. *et al.* Identification of microcephalin, a protein implicated in determining the size of the human brain. *Am. J. Hum. Genet.* **71**, 136–142 (2002).
11. do Carmo Avides, M. & Glover, D.M. Abnormal spindle protein, Asp, and the integrity of mitotic centrosomal microtubule organizing centers. *Science* **283**, 1733–1735 (1999).
12. Bi, W. *et al.* Increased LIS1 expression affects human and mouse brain development. *Nat. Genet.* **41**, 168–177 (2009).
13. Faulkner, N.E. *et al.* A role for the lissencephaly gene LIS1 in mitosis and cytoplasmic dynein function. *Nat. Cell Biol.* **2**, 784–791 (2000).
14. Reiner, O. *et al.* Isolation of a Miller-Dieker lissencephaly gene containing G protein β-subunit-like repeats. *Nature* **364**, 717–721 (1993).
15. Griffith, E. *et al.* Mutations in pericentrin cause Seckel syndrome with defective ATR-dependent DNA damage signaling. *Nat. Genet.* **40**, 232–236 (2008).
16. O'Driscoll, M., Ruiz-Perez, V.L., Woods, C.G., Jeggo, P.A. & Goodship, J.A. A splicing mutation affecting expression of ataxia-telangiectasia and Rad3-related protein (ATR) results in Seckel syndrome. *Nat. Genet.* **33**, 497–501 (2003).
17. Rauch, A. *et al.* Mutations in the pericentrin (PCNT) gene cause primordial dwarfism. *Science* **319**, 816–819 (2008).
18. Matera, I. *et al.* A sensitized mutagenesis screen identifies Gli3 as a modifier of Sox10 neurocristopathy. *Hum. Mol. Genet.* **17**, 2118–2131 (2008).
19. Diem, M.D., Chan, C.C., Younis, I. & Dreyfuss, G. PYM binds the cytoplasmic exon-junction complex and ribosomes to enhance translation of spliced mRNAs. *Nat. Struct. Mol. Biol.* **14**, 1173–1179 (2007).
20. Kataoka, N., Diem, M.D., Kim, V.N., Yong, J. & Dreyfuss, G. Magoh, a human homolog of *Drosophila* mago nashi protein, is a component of the splicing-dependent exon-exon junction complex. *EMBO J.* **20**, 6424–6433 (2001).
21. Le Hir, H., Gatfield, D., Braun, I.C., Forler, D. & Izaurralde, E. The protein Mago provides a link between splicing and mRNA localization. *EMBO Rep.* **2**, 1119–1124 (2001).
22. Nott, A., Le Hir, H. & Moore, M.J. Splicing enhances translation in mammalian cells: an additional function of the exon junction complex. *Genes Dev.* **18**, 210–222 (2004).
23. Palacios, I.M., Gatfield, D., St. Johnston, D. & Izaurralde, E. An eIF4AIII-containing complex required for mRNA localization and nonsense-mediated mRNA decay. *Nature* **427**, 753–757 (2004).
24. Pawlisz, A.S. *et al.* Lis1-Nde1-dependent neuronal fate control determines cerebral cortical size and lamination. *Hum. Mol. Genet.* **17**, 2441–2455 (2008).
25. Gambello, M.J. *et al.* Multiple dose-dependent effects of Lis1 on cerebral cortical development. *J. Neurosci.* **23**, 1719–1729 (2003).
26. Yingling, J. *et al.* Neuroepithelial stem cell proliferation requires Lis1 for precise spindle orientation and symmetric division. *Cell* **132**, 474–486 (2008).
27. Micklem, D.R. *et al.* The mago nashi gene is required for the polarisation of the oocyte and the formation of perpendicular axes in *Drosophila*. *Curr. Biol.* **7**, 468–478 (1997).
28. Azzalin, C.M. & Lingner, J. The human RNA surveillance factor UPF1 is required for S phase progression and genome stability. *Curr. Biol.* **16**, 433–439 (2006).
29. van der Weele, C.M., Tsai, C.W. & Wolniak, S.M. Mago nashi is essential for spermatogenesis in Marsilea. *Mol. Biol. Cell* **18**, 3711–3722 (2007).
30. Yamada, M. *et al.* Inhibition of calpain increases LIS1 expression and partially rescues *in vivo* phenotypes in a mouse model of lissencephaly. *Nat. Med.* **15**, 1202–1207 (2009).
31. Mulatinho, M., Llerena, J., Leren, T.P., Rao, P.N. & Quintero-Rivera, F. Deletion (1)(p32.2-p32.3) detected by array-CGH in a patient with developmental delay/mental retardation, dysmorphic features and low cholesterol: A new microdeletion syndrome? *Am. J. Med. Genet. A.* **146A**, 2284–2290 (2008).
32. Brunetti-Pierri, N. *et al.* Recurrent reciprocal 1q21.1 deletions and duplications associated with microcephaly or macrocephaly and developmental and behavioral abnormalities. *Nat. Genet.* **40**, 1466–1471 (2008).
33. Mefford, H.C. *et al.* Recurrent rearrangements of chromosome 1q21.1 and variable pediatric phenotypes. *N. Engl. J. Med.* **359**, 1685–1699 (2008).

ONLINE METHODS

Mapping and sequencing of mutations. Initial mapping of *Mos2* was done as described by using hypopigmentation as the criterion for affected mice[18]. For fine mapping, both affected and unaffected mice were genotyped by using simple sequence length polymorphisms (SSLP) markers and single-nucleotide polymorphisms (SNPs) that were polymorphic between BALB/cJ and C57BL/6J strains. *P* values were calculated by χ^2 analyses. PCR and sequencing of genomic DNA were done by the Harvard Partners Healthcare Center for Genetics and Genomics, Harvard Medical School.

Quantification. The thickness of the cortex, ventricular zone (Pax6-positive layer), intermediate zone and cortical plate (TuJ1-positive layer), and E18.5 neuronal layers was measured from confocal micrographs by using Zeiss AIM software. Measurements of E18.5 length and width were made from micrographs. BrdU-, Tuj1-, Tbr2- and Pax6-positive cells were quantified from confocal micrographs by using Image-Pro Plus v6.3 (MediaCybernetics) and ImageJ (http://rsb.info.nih.gov/ij; NIH) software. For analysis of E12.5 cortical cultures, only cells that were TuJ1-positive and Pax6-negative were included in the measurements. For this analysis, the average value was measured for $n = 3$ embryos of each genotype, or $n = 3345$ cells and $n = 2457$ cells for control and $Magoh^{Mos2/+}$ genotypes, respectively. Measurements of co-localization in cells (Tbr2 and BrdU, Tbr2 and GFP) were made by using Adobe Photoshop CS3. Mitotic orientation of dividing NSCs was calculated on micrographs by measuring the angle of chromosomes relative to the ventricle, as detected by using DAPI and anti-PH3 staining to mark prophase and metaphase cells and either a cytoplasmic marker or membrane marker to visualize the ventricular surface. Centrosome distances were calculated from confocal *z* stacks (0.44-μm slices) using ImagePro6.3 software. Centrosome distances were calculated on the following spindles: scrambled bipolar ($n = 268$), scrambled monopolar ($n = 12$), *Magoh* bipolar ($n = 201$) and *Magoh* monopolar ($n = 143$). For measurement of the average centrosome distance of all siRNA-treated cells, scrambled ($n = 280$) and *Magoh* ($n = 345$) cells were analyzed. Centrosome number was calculated from visual inspection of confocal *z* stacks. For analysis of monopolar spindles, the following number of cells were evaluated: scrambled ($n = 281$ cells), *Magoh* ($n = 629$ cells), *Rbm8a* ($n = 340$ cells), *Eif4a3* ($n = 335$ cells) and *Casc3* ($n = 235$ cells). Analysis of γ-H2AX–positive cells in sections was calculated within a 350-μm^2 field. For all siRNA analyses, significance was calculated relative to the scrambled control. For *in utero* electroporation experiments, GFP-positive cell location was quantified from confocal micrographs by dividing the cortex into five equal bins using Adobe Photoshop CS3. For each genotype, all staining was repeated on several sections taken from at least three independent embryos.

Mouse genetics and husbandry. The $Magoh^{Mos2/+}$ line was generated as described and maintained on a C57BL/6 background[18]. $Magoh^{GT0150/+}$ and $Magoh^{GT027/+}$ mice were generated from embryonic stem (ES) cells containing gene-trap insertions from Sanger. In brief, chimeras were made by injecting four to six ES cells into eight-cell stage C57BL/6 embryos, and blastocysts were injected into pseudo-pregnant C57BL/6 females. Chimeras with high ES cell contribution (evaluated by coat color) were crossed to C57BL/6 mice and evaluated for germline transmission. BAC constructs were purchased from the Children's Hospital Oakland Research Institute and purified with CsCl (Lofstrand Labs). Tg-BAC1 and Tg-BAC2 lines were made by injecting RP24-175K18 and RP23-274G4 BAC constructs, respectively, into C57BL/6 blastocysts. For this study, we used C57BL/6 inbred mice (purchased from The Jackson Laboratory) as a control and outcrossed $Magoh^{Mos2/+}$mice (>10 generations on C57BL/6J). BrdU injections were done intraperitoneally (50 μg per g body weight). For embryo collection, a gestation of 0.5 d (E0.5) was designated on identification of a plug in a female. All of the mice described were bred and housed in an NHGRI animal facility according to NIH guidelines. Animal care was done in accordance with NHGRI institutional standards and was approved by the Institutional Animal Care and Use Committee, NHGRI and NIH Institutional Review Board.

Genotyping. $Magoh^{Mos2/+}$mice were genotyped by using a real-time PCR Taqman SNP genotyping assay on an ABIPrism7000 instrument. For this assay, a region containing the point mutation was amplified by PCR. Two fluorescently labeled single-stranded oligonucleotides (probes), one complementary to the wild-type product and one complementary to the mutant product, were multiplexed in the assay. Allelic discrimination was performed to detect the relative amount of each allele at the conclusion of the PCR reaction. The following cycling conditions were used: step 1, 50 °C for 2 min; step 2, 95 °C for 10 min; step 3, 92 °C for 30 s; step 4, 60 °C for 60 s (repeat steps 3–4 for 40 cycles). The following primers and probes were used: 5′-GGCCCCTTTAGGCTCATACATTTTA-3′ (forward), 5′-ATCAATAATTCTCTTTAACTCTTCCATCACACT-3′ (reverse), 5′-CACATAAGCCTGCAATC-3′ (VIC probe, C57BL/6 allele), and 5′-CACATAAGCTGCAATC-3′ (FAM probe, $Magoh^{Mos2}$ allele; designed with Applied Biosystems software). BAC mice were genotyped by traditional PCR to detect the presence of the BAC construct in genomic DNA by using the following cycling conditions: step 1, 94 °C for 3 min; step 2, 93 °C for 30 s; step 3, 58 °C for 30 s; step 4, 72 °C for 30 s (repeating steps 2–4 for 35 cycles); step 5, 72 °C for 7 min. The following primers were used: 5′-CGCTGCAAAACGCTGACGGAACAGTAG-3′ (forward) and 5′-CTCAGCGTATGGTTGTCGCCGGATGTAT-3′ (reverse).

RT-PCR and sequencing. RNA from E10.5 or E12.5 cortex was used for first-strand cDNA synthesis with a High Capacity cDNA Reverse Transcription kit (ABI) used in accordance with the manufacturer's instructions. PCR amplification was subsequently done by using primers within exon 1 and 4 and the following conditions: step 1, 94 °C for 3 min; step 2, 94 °C for 30 s; step 3, 57 °C for 90 s; step 4, 72 °C for 30 s (repeating steps 2–4 for 35 cycles); step 5, 72 °C for 10 min. We used the following primers: 5′-CGTTACTACGTGGGCCACAA-3′ (forward) and 5′-GGTTGACATCAATAAGGGAACC-3′ (reverse). RT-PCR products were digested with AluI (New England Biolabs) before gel electrophoresis. Site-directed mutagenesis was used to generate a mutant *Magoh* cDNA construct containing the point nucleotide deletion (198delG) found in *Mos2* mutants (New England Biolabs). RT-PCR products from wild-type and mutant cortices were commercially sequenced (ACGT) with Big Dye terminator cycle sequencing reagents (ABI). For both the AluI digest and for sequencing, a mock heterozygote cDNA sample was generated as a control by combining wild-type and mutant cDNA plasmid DNA in a 1:1 mix before PCR amplification.

Quantitative gene expression. Gene expression was measured in E10.5 and E12.5 cortical RNA by using the following Taqman real-time PCR gene expression assays: *Magoh* (Mm00487546_m1), *Lis1* (*Pafah1b1*, Mm00443070_m1), *Pax6* (Mm00443081_m1) and *Tbr2* (*Eomes*; Mm01351984_m1). Expression was measured relative to a standard curve diluted from wild-type E12.5 embryonic head control cDNA. The expression in each sample was normalized to *Gapdh* expression measured by the same standard curve, and wild-type levels were set to 1.0. We carried out 20-μl reactions in 1× Fast Universal PCR Master Mix (ABI) with the following cycle conditions: step 1, 95 °C for 20 s; step 2, 95 °C for 3 s; step 3, 60 °C for 30 s (repeat steps 2–3 for 40 cycles). For all expression data, graphs were averaged from 3–4 replicate reactions for each of four to six control and $Magoh^{Mos2/+}$ cortices.

Metaphase and SKY analyses. Metaphase preparations were performed by a standard air-drying technique[34]. Fluorescent *in situ* hybridization was performed with DNA labeled with Spectrum Orange (Vysis) by a nick translation technique, essentially as described[35,36]. SKY analysis was done as described[37,38].

Immunoblot analyses and quantification. E10.5 and E12.5 cortices were dissected and frozen at −80 °C. $Magoh^{Mos2/+}$ and control cortices from the same litter were pooled and lysed in RIPA lysis buffer containing protease inhibitors (Pierce). Cortical extracts of mutant and wild-type samples from multiple litters were run on either 16% or 4–12% SDS-polyacrylamide gels (Invitrogen) and analyzed by immunoblotting using the following primary antibodies: mouse anti-Magoh (diluted 1:100; Santa Cruz), rabbit anti-Magoh (1:100; Abcam), mouse anti-Lis1 (1:1,000; Sigma), and mouse anti–α-tubulin (1:1,000; Sigma). The secondary antibodies (1:20,000) were anti–rabbit HRP and anti–mouse HRP (Amersham). Immunoblots were quantified by densitometry (Image J). Values for each lane were first normalized to α-tubulin, and the average ratio of mutant to wild-type was calculated for each blot. For Lis1 measurements, data were averaged from three blots including 8 litters (eight wild-type, eight mutant samples) for E10.5, and from seven blots including 13 litters (12 wild-type, 11 mutant samples) for E12.5. Samples were run in replicates of one to three blots.

Cell culture analysis and immunofluorescence. HeLa cells were grown to ~55% confluency and transfected with 50 nM siRNA (or 12 nM for each of four

siRNAs, or 6 nM for each of eight siRNAs; Qiagen) by using siLentFect (Bio-Rad). Cells were grown for 48 h and then either collected for FACS cell cycle analysis or immunoblot analysis, or plated onto chamber slides for an additional 12 h. Expression of both *Magoh* and *Magoh2* (a homolog with 99% amino acid identity) was targeted, because HeLa cells express both genes. The following siRNAs were used: control, AllStars Negative siRNA; *Magoh1*, Hs_Magoh_1, Hs_Magoh_2, Hs_Magoh_5 and Hs_Magoh_6; *Magoh2*, Hs_FLJ10292_6, Hs_FLJ10292_7, Hs_FLJ10292_8 and Hs_FLJ10292_9; *Rbm8a*, Hs_Rbm8a_1, Hs_Rbm8a_5, Hs_Rbm8a_6 and Hs_Rbm8a_7; *Eif4a3*, Hs_Eif4a3_2, Hs_Eif4a3_3, Hs_Eif4a3_5 and Hs_Eif4a3_6; and *Casc3*: Hs_Casc3_5, Hs_Casc3_6, Hs_Casc3_7 and Hs_Casc3_8. RPE cells were transfected with 100 nM siRNAs by using Lipofectamine 2000 (Invitrogen). Cells were treated at 0 and 24 h. RNA was collected at 48 h, and cells were fixed and stained at 72 h. Dissociated cortical cultures were prepared from E12.5 embryos and stained as described[39]. HeLa cells were plated onto coverslips and subconfluent cells were fixed in methanol at −20 °C for 20 min, and stained as described[40]. The following mouse antibodies were used: mouse anti–α-tubulin (diluted 1:500; Sigma), mouse anti-TuJ1 (1:1,000), rabbit anti–γ-tubulin (1:500; Sigma), anti–γ-H2AX (1:2,000; Millipore) and rabbit anti-Pax6 (1:2,000; Millipore). Analysis was done by using the microscopes described below.

Staining of mouse sections. Embryos (E12.5 and younger) or brains (E13.5 and older) were dissected and fixed overnight in 4% paraformaldehyde, washed in PBS, soaked sequentially in 10 and 20% sucrose overnight, and frozen in NEG-50 medium (Richard-Allan Scientific). Coronal sections (12–19-μm thick) were prepared by using a Leica CM3050S cryostat and staining was performed after blocking in 10% normal goat serum for rabbit, rat and goat primary antibodies or in MOM block (Vector laboratories) for mouse primary antibodies (1–2 h at 25 °C). Primary antibodies (either 2 h at 25 °C or overnight at 4 °C) and secondary antibodies (15 min at 25 °C) were diluted in normal goat serum or MOM diluent. For staining of nuclear antigens, sections were first permeabilized with 0.25% Triton X-100 for 10 min. For BrdU staining, sections were first heated at 55 °C in 1 M HCl for 15 min, or for double immunofluorescence were boiled in Citric Acid Antigen Unmasking solution (Vector Laboratories) for 30 min. Stained sections were mounted by using Vectashield with DAPI or with propidium iodide (Vector Laboratories). Stained sections were analyzed primarily with a Zeiss510LSM NLO confocal microscope with Meta Detector and also with a Zeiss Fluorescence Axioskop2 microscope with IPLab imaging software. Images were cropped as necessary by using Adobe Photoshop CS3. We used the following antibodies: rabbit, anti-CC3 (diluted 1:200; Cell Signaling), anti-PH3 (1:200; Upstate Biotechnology), anti-Magoh (1:200; Proteintech), anti-Cux1 (1:100; Santa Cruz), anti-Foxp1 (1:200; Abcam), anti-Foxp2 (1:100; Abcam), anti-Tbr1 (1:500; Abcam), anti-Tbr2 (1:1,000; Abcam), anti-Calretinin (1:200; Millipore) and anti-Pax6 (1:1,000; Millipore); mouse, anti-TuJ1 (1:400; Covance); goat, anti-doublecortin (1:50, Santa Cruz), anti–γ-H2AX (1:2,000, Millipore); and rat: anti-BrdU (1:200, Abcam). The secondary antibodies were Alex Fluor 488, Alex Fluor 568 and Alex Fluor 594 (1:200; Invitrogen) and mouse anti-HRP (Roche). TUNEL staining was done in accordance with the manufacturer's directions using an Apoptag fluorescein *in situ* apoptosis kit (Millipore). Nissl, and hematoxylin and eosin staining of paraffin sections was done by standard procedures (Histoserv). *In situ* hybridization images were taken from GenePaint[41].

***In utero* electroporation**. Gene transfer into embryonic CD1 mice was done by *in utero* electroporation as described with the Nepagene CUY21EDIT electroporator[42]. E13.5 embryos were electroporated with 3.7 μg of DNA in a total volume of 1 μl (2 μg of either pSM2-Luciferase-shRNA (RHS1705) or pSM2c-*Magoh*-shRNA (RMM1766-984609047), accompanied by 0.7 μg of pCAGGS-GFP and, as noted, 1 μg each of pCAGGS-*Lis1* and either empty vector or pCLE-IRES-Plap). Either pCAG or pCLE was used as an empty vector with similar results. E16.5 embryonic brains were prepared as described above. shRNAs were purchased from Open Biosystems. *Lis1* was subcloned into a pCAGGS vector from a pcDNA3-*Lis1* construct (Addgene). Graphs include analyses of the following: luciferase shRNA plus vector ($n = 13$ sections, five brains), *Magoh* shRNA plus vector ($n = 13$ sections, four brains), *Magoh* shRNA plus *Lis1* ($n = 22$ sections, eight brains), and luciferase shRNA plus *Lis1* ($n = 22$ sections, nine brains). For quantification of Tbr2-positive, GFP-positive cells, the analysis included $n = 13$–22 sections and $n = 4$–9 brains for each electroporation.

Microarray and proteomic analyses. We carried out microarray analysis as described using five biological replicates each of RNA prepared from E10.5 $Magoh^{Mos2/+}$ and control cortices[43]. To ensure reproducible dissections, the olfactory epithelium was included in cortical dissections. Proteomic analyses were done with three biological replicates each of protein prepared from $Magoh^{Mos2/+}$ and control cortices. Proteomic analyses and statistical analyses of data were performed by Applied Biomics.

Statistical analysis. **Supplementary Table 3** lists all of the statistical tests used for data analysis and the actual *P* values calculated.

34. Lundsteen, C. & Lind, A.M. A test of a climate room for preparation of chromosome slides. *Clin. Genet.* **28**, 260–262 (1985).
35. Lichter, P., Cremer, T., Borden, J., Manuelidis, L. & Ward, D.C. Delineation of individual human chromosomes in metaphase and interphase cells by *in situ* suppression hybridization using recombinant DNA libraries. *Hum. Genet.* **80**, 224–234 (1988).
36. Pinkel, D., Straume, T. & Gray, J.W. Cytogenetic analysis using quantitative, high-sensitivity, fluorescence hybridization. *Proc. Natl. Acad. Sci. USA* **83**, 2934–2938 (1986).
37. Liyanage, M. *et al.* Multicolour spectral karyotyping of mouse chromosomes. *Nat. Genet.* **14**, 312–315 (1996).
38. Schrock, E. *et al.* Multicolor spectral karyotyping of human chromosomes. *Science* **273**, 494–497 (1996).
39. Gaiano, N., Nye, J.S. & Fishell, G. Radial glial identity is promoted by Notch1 signaling in the murine forebrain. *Neuron* **26**, 395–404 (2000).
40. Kittler, R. *et al.* An endoribonuclease-prepared siRNA screen in human cells identifies genes essential for cell division. *Nature* **432**, 1036–1040 (2004).
41. Visel, A., Thaller, C. & Eichele, G. GenePaint.org: an atlas of gene expression patterns in the mouse embryo. *Nucleic Acids Res.* **32**, D552–D556 (2004).
42. Saito, T. *In vivo* electroporation in the embryonic mouse central nervous system. *Nat. Protocols* **1**, 1552–1558 (2006).
43. Buac, K. *et al.* NRG1 / ERBB3 signaling in melanocyte development and melanoma: inhibition of differentiation and promotion of proliferation. *Pigm. Cell Melanoma Res.* **22**, 773–784 (2009).

doi:10.1038/nn.2527